## Evidence of Topological Hall Effect in Pt/Antiferromagnetic-Insulator Bilayers

Yang Cheng<sup>1,\*</sup>, Sisheng Yu<sup>1,\*</sup>, Menglin Zhu<sup>2</sup>, Jinwoo Hwang<sup>2</sup>, Fengyuan Yang<sup>1</sup>

<sup>1</sup>Department of Physics, The Ohio State University, Columbus, OH, 43210, USA

<sup>2</sup>Department of Materials Science and Engineering, The Ohio State University, Columbus, OH, 43212, USA

\*These two authors contributed equally to this work.

## Abstract

Topological Hall effect has been a primary indicator of non-trivial spin textures in magnetic materials. We observe the evidence of topological Hall effect in Pt/Cr<sub>2</sub>O<sub>3</sub> bilayers grown on  $Al_2O_3(0001)$  and  $Al_2O_3(11\bar{2}0)$ , where  $Cr_2O_3$  epitaxial film is an antiferromagnetic insulator. The Pt/Cr<sub>2</sub>O<sub>3</sub> bilayers exhibit topological Hall resistivity for  $Cr_2O_3$  thicknesses below 6 nm near and above room temperature, which is above the Néel temperature of  $Cr_2O_3$ , revealing the key role of thermal fluctuations in the formation of spin textures. The similarity of topological Hall signals in (0001)- and  $(11\bar{2}0)$ -oriented  $Cr_2O_3$  films indicates that the emergence of spin textures is insensitive to crystalline orientation.

Topological spin textures, such as skyrmions, have attracted intense interest in recent years. <sup>1-8</sup> The competition between exchange interaction, magnetic anisotropy, and Dzyaloshinskii-Moriya interaction (DMI) generates chiral spin textures in bulk non-centrosymmetric materials <sup>9</sup> and magnetic multilayers. <sup>10</sup> Electric transport measurement via the topological Hall (TH) effect is a powerful tool for detecting spin textures. In conducting skyrmion materials, the TH effect arises when electrons flowing in the spin textures experience an emergent electromagnetic field through interaction with the textured spins <sup>1</sup> and are scattered off of the textures, producing a uniquely identifiable TH voltage. <sup>11</sup>

Magnetic skyrmions have been studied almost exclusively in bulk ferromagnets (FM) or FM multilayers. Antiferromagnets  $(AF)^{12-14}$  have also been predicted to harbor topological spin textures such as AF skyrmions. To date, except some non-collinear AFs with intrinsic chirality, where the AFs solely play an auxiliary role, such as providing an exchange bias or an AF heavy metal (HM) to generate a large interfacial DMI while spin chirality emerges in the neighboring layer. Recently, thermally-driven spin chirality fluctuations have been predicted in materials with spin frustrations and verified in 2D Ising FMs even above their Curie temperatures ( $T_C$ ). Here, we report the detection of topological spin textures in Pt/Cr2O3 bilayers using TH effect near and above the Néel temperature ( $T_N$ ) of AF insulator (AFI) Cr2O3 films.

Epitaxial Cr<sub>2</sub>O<sub>3</sub> thin films are grown on Al<sub>2</sub>O<sub>3</sub>(0001) and Al<sub>2</sub>O<sub>3</sub>(11 $\overline{2}$ 0) substrates using offaxis sputtering at a substrate temperature of 500°C.<sup>24-27</sup> Figure 1(a) shows  $2\theta/\omega$  X-ray diffraction (XRD) scans for Cr<sub>2</sub>O<sub>3</sub>(30 nm) films on Al<sub>2</sub>O<sub>3</sub>(0001) and Al<sub>2</sub>O<sub>3</sub>(11 $\overline{2}$ 0). Figure 1(b) shows an XRD rocking curve of the Cr<sub>2</sub>O<sub>3</sub> (0006) peak for the (0001)-oriented film [the (11 $\overline{2}$ 0)-oriented film gives a similar rocking curve]. The clear Laue oscillations and narrow full-width-at-half-maximum (FWHM) of the rocking curves indicate the high crystal quality of the Cr<sub>2</sub>O<sub>3</sub> films in both orientations. Figure 1(c) shows an X-ray reflectometry (XRR) scan of the Cr<sub>2</sub>O<sub>3</sub> film on Al<sub>2</sub>O<sub>3</sub>(0001), where the fitting gives a roughness of 0.1 nm. The smooth surface is confirmed by atomic force microscopy (AFM) as shown in Fig. 1(d) with a roughness of 0.1 nm. The scanning transmission electron microscopy image for a 30 nm Cr<sub>2</sub>O<sub>3</sub> film on Al<sub>2</sub>O<sub>3</sub>(0001) in Fig. 1(e) reveals the epitaxy and single crystal ordering of Cr<sub>2</sub>O<sub>3</sub>.

Given that  $Cr_2O_3$  is insulating, the predicted topological spin textures in the AF, if exist, cannot be directly detected electrically. We deposit a 2 nm Pt layer on  $Cr_2O_3$  films of various thicknesses (t) at room temperature using off-axis sputtering, where the Pt layer provides a channel for Hall measurement as well as interfacial DMI needed for the formation of spin textures. The  $Pt(2 \text{ nm})/Cr_2O_3(t)$  bilayers are patterned into Hall bars with a current channel width of 100  $\mu$ m.

Figure 2(a) shows the Hall resistivity for a Pt(2 nm)/Cr<sub>2</sub>O<sub>3</sub>(5 nm) bilayer on Al<sub>2</sub>O<sub>3</sub>(0001) at a temperature (T) of 345 K with an out-of-plane field (H) and a DC current of 100 μA. In general, there are three terms in the Hall resistivity,  $\rho_{xy} = \rho_{OH} + \rho_{AH} + \rho_{TH}$ , including the ordinary Hall ( $\rho_{OH}$ ), anomalous Hall ( $\rho_{AH}$ ), and topological Hall ( $\rho_{TH}$ ) resistivities.<sup>7, 28</sup>  $\rho_{OH}$  has a linear field dependence. At 345 K,  $\rho_{AH}$  in the Pt/Cr<sub>2</sub>O<sub>3</sub> bilayer is due to the spin-Hall anomalous Hall effect (SH-AHE).<sup>29, 30</sup> Since 345 K is higher than the  $T_N = 307$  K<sup>31</sup> of bulk Cr<sub>2</sub>O<sub>3</sub> and ~280 K for 20 nm Cr<sub>2</sub>O<sub>3</sub>(0001),<sup>32</sup> we use the Langevin function to fit the SH-AHE data as shown in Fig. 2(a), which agrees well with the experimental data at |H| < 0.2 T and |H| > 1.4 T. However, there is a pronounced upturn at 0.2 T < |H| < 1.4 T that cannot be explained by the SH-AHE. We think it is very likely that the topological Hall effect (THE) leads to this upturn feature, which can be extracted by subtracting the OHE and SH-AHE. The obtained  $\rho_{TH}$  vs. H plot is presented in Fig. 2(b), which shows a TH region within |H| < 1.4 T with a peak value of 0.45 nΩ cm at ±0.4 T and

sign switching at H = 0.

Following the same process, we measure  $\rho_{xy}$  of the Pt(2 nm)/Cr<sub>2</sub>O<sub>3</sub>(5 nm) bilayer on Al<sub>2</sub>O<sub>3</sub>(0001) from T = 250 to 385 K and fit the data using the Langevin function, as shown in Fig. 2(c). Figure 2(d) shows the corresponding  $\rho_{TH}$  vs. H plots and the inset gives the temperature dependence of  $\rho_{TH}$ , which indicate that  $\rho_{TH}$  disappears below 300 K and above 365 K. The observed THE in our Pt/Cr<sub>2</sub>O<sub>3</sub> bilayer indicates spin chirality in the Cr<sub>2</sub>O<sub>3</sub> film, which is attributed to the DMI at the Pt/Cr<sub>2</sub>O<sub>3</sub> interface (For more details about the DMI at Pt/Cr<sub>2</sub>O<sub>3</sub> interface, see *Supplementary Materials*). The spin chirality at  $T > T_C$  has been observed in FM SrRuO<sub>3</sub> and V-doped Sb<sub>2</sub>Te<sub>3</sub>,<sup>23</sup> which was explained as spin chirality fluctuations in quasi-two-dimensional FMs with weak DMI. Unlike the FMs where the THE appears within a small temperature window near and above  $T_C$ , the THE in the AF Cr<sub>2</sub>O<sub>3</sub> films is robust even at 60 K above its bulk  $T_N$ .

We next conduct Hall measurement for various  $Cr_2O_3$  thicknesses at 345 K, as shown in Figs. 3(a) and 3(b). The TH peaks persist at t = 3 to 5 nm and disappear at 6 nm. Besides, the  $\rho_{TH}$  peak position moves from 0.8 to 0.4 T as t increases from 3 to 5 nm.<sup>23</sup> Figure 3(c) shows the thickness dependence of  $\rho_{TH}$ , which drops suddenly to zero from 5 to 6 nm, indicating that the DMI is not large enough to stabilize spin textures in thicker  $Cr_2O_3$  films.<sup>23</sup> Figure 3(e) summarizes the temperature-thickness phase diagram of  $\rho_{TH}$  for the Pt/Cr<sub>2</sub>O<sub>3</sub> bilayers on Al<sub>2</sub>O<sub>3</sub>(0001).

To better understand the observed THE, we use Monte-Carlo (MC) simulations to model the spin textures. Cr<sub>2</sub>O<sub>3</sub> has a corundum structure and a rhombohedral unit cell. According to neutron measurements and first-principle calculations,<sup>33, 34</sup> the first and second-nearest neighbor exchange coupling constants,  $J_1$  and  $J_2$ , are dominant. Thus, the Hamiltonian can be written as,  $H = -\sum_{\langle i,j \rangle} J_1\left(S_i \cdot S_j\right) - \sum_{\langle k,l \rangle} J_2\left(S_k \cdot S_l\right) + \sum_{\langle i,j \rangle} D_{ij} \cdot \left(S_i \times S_j\right) - B_z \sum_i S_i^z - K \sum_i (S_i^z)^2, \quad (1)$ where S is the unit spin vector, the third term is the DMI, the fourth term is the Zeeman energy,

and the last term is the uniaxial anisotropy along  $Cr_2O_3(0001)$ . We choose  $J_1 = -1$ ,  $J_2 = -0.74$  based on first-principle calculations, and K = 1. D ranges from 0.1 to 0.5 to simulate DMI of different  $Cr_2O_3$  thicknesses, which forbids spin chirality at low temperatures. We use six layers with 31 × 31 spins in each layer to rebuild the exchange coupling in the  $Cr_2O_3$  rhombohedral unit cell along (0001) with the periodic boundary condition. The DMI is only exerted on the first layer and the spin chirality is indicated by the topological charge Q of the top layer<sup>22</sup>

$$Q = \frac{1}{4\pi} \int d^2 \mathbf{r} \mathbf{S} \cdot (\partial_x \mathbf{S} \times \partial_y \mathbf{S}), \tag{2}$$

which can be calculated by the summation of the solid angle determined by three neighboring unit spin vectors in the first layer of spin lattice.<sup>35</sup> Figure 3(d) shows the field dependence of Q at D = 0.5 and T = 1.05  $T_N$ , where  $T_N$  is determined by the temperature dependence of susceptibility  $\chi$  through MC simulation.<sup>36</sup> The antisymmetric curve of Q in Fig. 3(d) for Cr<sub>2</sub>O<sub>3</sub> is similar to the reported simulations for FMs.<sup>23</sup> Since  $\rho_{TH} \propto Q$ , our simulations confirm the presence of spin chirality at  $T > T_N$ . Figure 3(f) summarizes the phase diagram of Q for Cr<sub>2</sub>O<sub>3</sub>(0001) with varying T and  $T_N = T_N = T_N$ 

Cr<sub>2</sub>O<sub>3</sub> is a uniaxial AF with spins aligned along the easy axis [0001]. To explore how the crystallographic and spin orientations affect the formation of spin textures, we perform the same measurements of  $\rho_{xy}$  for Pt/Cr<sub>2</sub>O<sub>3</sub> bilayers grown on Al<sub>2</sub>O<sub>3</sub>(11 $\bar{2}$ 0) with an in-plane easy axis. Figure 4(a) shows the  $\rho_{xy} - \rho_{OH}$  vs. H data for a Pt(2 nm)/Cr<sub>2</sub>O<sub>3</sub>(5 nm) bilayer on Al<sub>2</sub>O<sub>3</sub>(11 $\bar{2}$ 0) from T = 250 to 385 K with are Langevin fitting for  $\rho_{AH}$ . The TH peaks are observed from 300 to 385 K, as compared to 325-365 K for Pt/Cr<sub>2</sub>O<sub>3</sub>(0001). In addition, the TH peak appears at smaller fields, 0.2 T at 345 K as compared to 0.4 T for Pt/Cr<sub>2</sub>O<sub>3</sub>(0001). Figure 4(b) shows the field dependence of  $\rho_{TH}$  obtained by subtracting the fitting curve of  $\rho_{AH}$  from  $\rho_{xy}$  -  $\rho_{OH}$ . The magnitude

of  $\rho_{TH}$  reaches the maximum at 325 K, as seen in the inset of Fig. 4(b). Surprisingly, there is small non-zero TH signal even at 385 K. The differences in the TH signals between the bilayers grown on (0001)- and (11 $\bar{2}$ 0)-orientated Al<sub>2</sub>O<sub>3</sub> may be attributed to the different magnitude of uniaxial anisotropy, and  $T_N$  due to strain,<sup>32, 38</sup> the direction of uniaxial anisotropy or spin configurations at the surface layer of Cr<sub>2</sub>O<sub>3</sub>. The detailed mechanism needs further exploration. However, we can conclude that the Pt/Cr<sub>2</sub>O<sub>3</sub>(11 $\bar{2}$ 0) bilayers share similar topological Hall features with the Pt/Cr<sub>2</sub>O<sub>3</sub>(0001) bilayers.

Figure 5(a) shows the thickness dependence of  $\rho_{xy} - \rho_{OH}$  for Pt/Cr<sub>2</sub>O<sub>3</sub>(t) bilayers on Al<sub>2</sub>O<sub>3</sub>(11 $\overline{2}0$ ) at 345 K, from which  $\rho_{TH}$  is extracted as shown in Fig. 5(b). The TH signal persists from 3 to 6 nm and vanishes at t = 10 nm. Meanwhile, the TH peak position is lowered from 0.6 to 0.2 T as t increases from 3 to 6 nm, which is similar to the Pt/Cr<sub>2</sub>O<sub>3</sub>(0001) bilayers. The magnitude of  $\rho_{TH}$  has the maximum at 3 nm and then gradually decreases as Cr<sub>2</sub>O<sub>3</sub> becomes thicker [Fig. 5(c)]. Figure 5(d) shows the MC simulation of topological charge Q in a varying out-of-plane field. For Cr<sub>2</sub>O<sub>3</sub>(11 $\overline{2}0$ ), we use four layers to rebuild the AF exchange coupling to the second-nearest neighbor. The last term in Eq. (1) is rewritten as  $-K \sum_i (S_i^x)^2$  because of the inplane easy axis. The similarity of Q between Cr<sub>2</sub>O<sub>3</sub>(11 $\overline{2}0$ ) and Cr<sub>2</sub>O<sub>3</sub>(0001) is consistent with our experimental results. Compared with the Cr<sub>2</sub>O<sub>3</sub>(0001) in Fig. 3(e), Cr<sub>2</sub>O<sub>3</sub>(11 $\overline{2}0$ ) has a broader T-t range for THE as shown in Fig. 5(e). Figure 5(f) shows the simulation, which indicates a larger phase space of Q, possibly due to the different crystal orientation and anisotropy.

The similar phase diagrams of spin textures in the Cr<sub>2</sub>O<sub>3</sub> films with different crystal and spin orientations indicate the minor role played by the uniaxial anisotropy. We believe the spin textures in our Pt/Cr<sub>2</sub>O<sub>3</sub> bilayers have similar fundamental origin as that in FM SrRuO<sub>3</sub> and V-doped Sb<sub>2</sub>Te<sub>3</sub>.<sup>23</sup> The broken inversion symmetry at the Pt/Cr<sub>2</sub>O<sub>3</sub> interface provides the DMI. Due

to the relatively small DMI at Pt/Cr<sub>2</sub>O<sub>3</sub> interface compared to the exchange interaction in Cr<sub>2</sub>O<sub>3</sub>,<sup>39</sup> spin textures can only emerge near or above T<sub>N</sub> with the assistance of thermal fluctuations to overcome the strong AF exchange interaction. In conducting FM or AF layers that exhibit THE, conduction electrons are deflected by the emergent electromagnetic field due to the spin chirality. Proximity effect<sup>40, 41</sup> in Pt/Cr<sub>2</sub>O<sub>3</sub> bilayers is another possibility to explain the mapping of spin textures from Cr<sub>2</sub>O<sub>3</sub> to Pt; while to date, the existence of proximity in Pt/Cr<sub>2</sub>O<sub>3</sub> is debatable<sup>41-43</sup> and it is unlikely to preserve the moment in Pt at  $T > T_{\rm N}$ .<sup>44</sup> We propose a new mechanism, spin Hall topological Hall effect (SH-THE), 45, 46 which is similar to the SH-AHE in Pt/FMI and AFI bilayers. The SH-THE arises from the following process: 1) as a current flows through the Pt layer, it generates spin accumulation via the spin Hall effect at the Pt/Cr<sub>2</sub>O<sub>3</sub> interface; 2) the spin accumulation exerts a spin torque on the AF moments in Cr<sub>2</sub>O<sub>3</sub>, which form spin textures at appropriate thickness and temperature range; 3) the spins in Pt at the interface experience a reaction torque from the winding AF spin textures in Cr<sub>2</sub>O<sub>3</sub> and acquire a Berry phase, resulting in a topological Hall effect. This process should apply to both FMI and AFI based bilayers. Similar SH-THE has also been observed in Pt/Tm<sub>3</sub>Fe<sub>5</sub>O<sub>12</sub> bilayers.<sup>46</sup>

In summary, we observe strong evidence of topological Hall effect in  $Pt/Cr_2O_3$  bilayers at temperatures near or above the  $T_N$ , revealing the emergence of spin textures in collinear AF insulator films. This first evidence of topological Hall effect in HM/AFI bilayers significantly expands our materials base to include the large family of AF insulators for the exploration of AF-based skyrmion technology.

This work was supported primarily by the US Department of Energy (DOE) under Grant No. DE-SC0001304. Partial support is provided by DARPA under Grant No. D18AP00008 (structural characterization).

## **References:**

- 1. N. Nagaosa and Y. Tokura, "Topological properties and dynamics of magnetic skyrmions," *Nat. Nanotechnol.* **8**, 899 (2013).
- 2. X. Z. Yu, N. Kanazawa, Y. Onose, K. Kimoto, W. Z. Zhang, S. Ishiwata, Y. Matsui and Y. Tokura, "Near room-temperature formation of a skyrmion crystal in thin-films of the helimagnet FeGe," *Nat. Mater.* **10**, 106 (2011).
- 3. K. Shibata, X. Z. Yu, T. Hara, D. Morikawa, N. Kanazawa, K. Kimoto, S. Ishiwata, Y. Matsui and Y. Tokura, "Towards control of the size and helicity of skyrmions in helimagnetic alloys by spin-orbit coupling," *Nat. Nanotechnol.* **8**, 723 (2013).
- 4. W. J. Jiang, P. Upadhyaya, W. Zhang, G. Q. Yu, M. B. Jungfleisch, F. Y. Fradin, J. E. Pearson, Y. Tserkovnyak, K. L. Wang, O. Heinonen, S. G. E. te Velthuis and A. Hoffmann, "Blowing magnetic skyrmion bubbles," *Science* **349**, 283 (2015).
- 5. L. Vistoli, W. B. Wang, A. Sander, Q. X. Zhu, B. Casals, R. Cichelero, A. Barthélémy, S. Fusil, G. Herranz, S. Valencia, R. Abrudan, E. Weschke, K. Nakazawa, H. Kohno, J. Santamaria, W. D. Wu, V. Garcia and M. Bibes, "Giant topological Hall effect in correlated oxide thin films," *Nat. Phys.* **15**, 67 (2019).
- 6. J. Matsuno, N. Ogawa, K. Yasuda, F. Kagawa, W. Koshibae, N. Nagaosa, Y. Tokura and M. Kawasaki, "Interface-driven topological Hall effect in SrRuO<sub>3</sub>-SrIrO<sub>3</sub> bilayer," *Sci. Adv.* **2**, e1600304 (2016).
- 7. J. C. Gallagher, K. Y. Meng, J. T. Brangham, H. L. Wang, B. D. Esser, D. W. McComb and F. Y. Yang, "Robust Zero-Field Skyrmion Formation in FeGe Epitaxial Thin Films," *Phys. Rev. Lett.* **118**, 027201 (2017).
- 8. A. Neubauer, C. Pfleiderer, B. Binz, A. Rosch, R. Ritz, P. G. Niklowitz and P. Boni, "Topological Hall Effect in the A Phase of MnSi," *Phys. Rev. Lett.* **102**, 186602 (2009).
- 9. N. Kanazawa, S. Seki and Y. Tokura, "Noncentrosymmetric Magnets Hosting Magnetic Skyrmions," *Adv. Mater.* **29**, 1603227 (2017).
- 10. A. Fert, N. Reyren and V. Cros, "Magnetic skyrmions: advances in physics and potential applications," *Nat. Rev. Mater.* **2**, 17031 (2017).
- 11. Y. Taguchi, Y. Oohara, H. Yoshizawa, N. Nagaosa and Y. Tokura, "Spin Chirality, Berry Phase, and Anomalous Hall Effect in a Frustrated Ferromagnet," *Science* **291**, 2573 (2001).
- 12. T. Kampfrath, A. Sell, G. Klatt, A. Pashkin, S. Mahrlein, T. Dekorsy, M. Wolf, M. Fiebig, A. Leitenstorfer and R. Huber, "Coherent terahertz control of antiferromagnetic spin waves," *Nat. Photonics* **5**, 31 (2011).
- 13. X. Marti, I. Fina, C. Frontera, J. Liu, P. Wadley, Q. He, R. J. Paull, J. D. Clarkson, J. Kudrnovsky, I. Turek, J. Kunes, D. Yi, J. H. Chu, C. T. Nelson, L. You, E. Arenholz, S. Salahuddin, J. Fontcuberta, T. Jungwirth and R. Ramesh, "Room-temperature antiferromagnetic memory resistor," *Nat. Mater.* 13, 367 (2014).
- 14. V. Baltz, A. Manchon, M. Tsoi, T. Moriyama, T. Ono and Y. Tserkovnyak, "Antiferromagnetic spintronics," *Rev. Mod. Phys.* **90**, 015005 (2018).
- 15. C. A. Akosa, O. A. Tretiakov, G. Tatara and A. Manchon, "Theory of the Topological Spin Hall Effect in Antiferromagnetic Skyrmions: Impact on Current-Induced Motion," *Phys. Rev. Lett.* **121**, 097204 (2018).
- 16. B. Göbel, A. Mook, J. Henk and I. Mertig, "Antiferromagnetic skyrmion crystals: Generation, topological Hall, and topological spin Hall effect," *Phys. Rev. B* **96**, 060406 (2017).
- 17. X. C. Zhang, Y. Zhou and M. Ezawa, "Antiferromagnetic Skyrmion: Stability, Creation and Manipulation," *Sci Rep* **6**, 24795 (2016).

- 18. C. Sürgers, G. Fischer, P. Winkel and H. v. Löhneysen, "Large topological Hall effect in the non-collinear phase of an antiferromagnet," *Nat. Commun.* **5**, 3400 (2014).
- 19. Q. L. He, G. Yin, L. Y. Yu, A. J. Grutter, L. Pan, C.-Z. Chen, X. Y. Che, G. Q. Yu, B. Zhang, Q. M. Shao, A. L. Stern, B. Casas, J. Xia, X. D. Han, B. J. Kirby, R. K. Lake, K. T. Law and K. L. Wang, "Topological Transitions Induced by Antiferromagnetism in a Thin-Film Topological Insulator," *Phys. Rev. Lett.* 121, 096802 (2018).
- 20. G. Q. Yu, A. Jenkins, X. Ma, S. A. Razavi, C. L. He, G. Yin, Q. M. Shao, Q. L. He, H. Wu, W. J. Li, W. J. Jiang, X. F. Han, X. Q. Li, A. C. Bleszynski Jayich, P. K. Amiri and K. L. Wang, "Room-Temperature Skyrmions in an Antiferromagnet-Based Heterostructure," *Nano Letters* 18, 980 (2018).
- 21. Y. L. Lu, X. Guo, V. Koval and C. L. Jia, "Topological thermal Hall effect driven by spin-chirality fluctuations in frustrated antiferromagnets," *Phys. Rev. B* **99**, 054409 (2019).
- 22. W.-T. Hou, J.-X. Yu, M. Daly and J. D. Zang, "Thermally driven topology in chiral magnets," *Phys. Rev. B* **96**, 140403 (2017).
- 23. W. B. Wang, M. W. Daniels, Z. L. Liao, Y. F. Zhao, J. Wang, G. Koster, G. Rijnders, C. Z. Chang, D. Xiao and W. D. Wu, "Universal spin chirality fluctuation in two-dimensional Ising ferromagnets," *arXiv:1812.07005* (2018).
- 24. A. J. Hauser, R. E. A. Williams, R. A. Ricciardo, A. Genc, M. Dixit, J. M. Lucy, P. M. Woodward, H. L. Fraser and F. Y. Yang, "Unlocking the potential of half-metallic Sr<sub>2</sub>FeMoO<sub>6</sub> films through controlled stoichiometry and double-perovskite ordering," *Phys. Rev. B* **83**, 014407 (2011).
- 25. B. Peters, A. Alfonsov, C. G. F. Blum, S. J. Hageman, P. M. Woodward, S. Wurmehl, B. Büchner and F. Y. Yang, "Epitaxial films of Heusler compound Co<sub>2</sub>FeAl<sub>0.5</sub>Si<sub>0.5</sub> with high crystalline quality grown by off-axis sputtering," *Appl. Phys. Lett.* **103**, 162404 (2013).
- 26. A. J. Lee, J. T. Brangham, Y. Cheng, S. P. White, W. T. Ruane, B. D. Esser, D. W. McComb, P. C. Hammel and F. Y. Yang, "Metallic Ferromagnetic Films with Magnetic Damping Under 1.4 x 10<sup>-3</sup>," *Nat. Commun.* **8**, 234 (2017).
- 27. F. Y. Yang and P. C. Hammel, "Topical review: FMR-Driven Spin Pumping in Y<sub>3</sub>Fe<sub>5</sub>O<sub>12</sub>-Based Structures," *J. Phys. D: Appl. Phys.* **51**, 253001 (2018).
- 28. S. X. Huang and C. L. Chien, "Extended Skyrmion Phase in Epitaxial FeGe(111) Thin Films," *Phys. Rev. Lett.* **108**, 267201 (2012).
- 29. Y. T. Chen, S. Takahashi, H. Nakayama, M. Althammer, S. T. B. Goennenwein, E. Saitoh and G. E. W. Bauer, "Theory of spin Hall magnetoresistance," *Phys. Rev. B* **87**, 144411 (2013).
- 30. Y. Ji, J. Miao, Y. M. Zhu, K. K. Meng, X. G. Xu, J. K. Chen, Y. Wu and Y. Jiang, "Negative spin Hall magnetoresistance in antiferromagnetic Cr<sub>2</sub>O<sub>3</sub>/Ta bilayer at low temperature region," *Appl. Phys. Lett.* **112**, 232404 (2018).
- 31. S. Foner, "High-Field Antiferromagnetic Resonance in Cr<sub>2</sub>O<sub>3</sub>," *Phys. Rev.* **130**, 183 (1963).
- 32. T. Lino, T. Moriyama, H. Iwaki, H. Aono, Y. Shiratsuchi and T. Ono, "Resistive detection of the Néel temperature of Cr<sub>2</sub>O<sub>3</sub> thin films," *Appl. Phys. Lett.* **114**, 022402 (2019).
- 33. K. Lee, Y. Youn and S. Han, "Identification of ground-state spin ordering in antiferromagnetic transition metal oxides using the Ising model and a genetic algorithm," *Sci. Technol. Adv. Mater.* **18**, 246 (2017).
- 34. E. J. Samuelsen, M. T. Hutchings and G. Shirane, "Inelastic neutron scattering investigation of spin waves and magnetic interactions in Cr<sub>2</sub>O<sub>3</sub>," *Physica* **48**, 13 (1970).

- 35. I. A. Iakovlev, O. M. Sotnikov and V. V. Mazurenko, "Supervised learning approach for recognizing magnetic skyrmion phases," *Phys. Rev. B* **98**, 174411 (2018).
- 36. A. K. Murtazaev, "Critical properties of the model of antiferromagnet Cr<sub>2</sub>O<sub>3</sub>," *Low Temp. Phys.* **25**, 344 (1999).
- 37. J. Cho, N.-H. Kim, S. Lee, J.-S. Kim, R. Lavrijsen, A. Solignac, Y. X. Yin, D.-S. Han, N. J. J. van Hoof, H. J. M. Swagten, B. Koopmans and C.-Y. You, "Thickness dependence of the interfacial Dzyaloshinskii–Moriya interaction in inversion symmetry broken systems," *Nat. Commun.* **6**, 7635 (2015).
- 38. Y. Kota, H. Imamura and M. Sasaki, "Strain-Induced Néel Temperature Enhancement in Corundum-Type Cr<sub>2</sub>O<sub>3</sub> and Fe<sub>2</sub>O<sub>3</sub>," *Appl. Phys. Express* **6**, 113007 (2013).
- 39. A. Belabbes, G. Bihlmayer, F. Bechstedt, S. Blügel and A. Manchon, "Hund's Rule-Driven Dzyaloshinskii-Moriya Interaction at 3d-5d Interfaces," *Phys. Rev. Lett.* **117**, 247202 (2016).
- 40. W. Amamou, I. V. Pinchuk, A. H. Trout, R. E. A. Williams, N. Antolin, A. Goad, D. J. O'Hara, A. S. Ahmed, W. Windl, D. W. McComb and R. K. Kawakami, "Magnetic proximity effect in Pt/CoFe<sub>2</sub>O<sub>4</sub> bilayers," *Phys. Rev. Mater.* **2**, 011401 (2018).
- 41. Y. Cheng, S. S. Yu, A. S. Ahmed, M. L. Zhu, J. Hwang and F. Y. Yang, "Anisotropic Magnetoresistance and Nontrivial Spin Magnetoresistance in Pt/α-Fe<sub>2</sub>O<sub>3</sub> Bilayers: Evidence for Antiferromagnetic Proximity Effect," *arXiv*:1906.04395 (2019).
- 42. S. Seki, T. Ideue, M. Kubota, Y. Kozuka, R. Takagi, M. Nakamura, Y. Kaneko, M. Kawasaki and Y. Tokura, "Thermal Generation of Spin Current in an Antiferromagnet," *Phys. Rev. Lett.* **115**, 266601 (2015).
- 43. N. Wu, X. He, A. L. Wysocki, U. Lanke, T. Komesu, K. D. Belashchenko, C. Binek and P. A. Dowben, "Imaging and Control of Surface Magnetization Domains in a Magnetoelectric Antiferromagnet," *Phys. Rev. Lett.* **106**, 087202 (2011).
- 44. S. Cao, M. Street, J. Wang, J. Wang, X. Zhang, C. Binek and P. A. Dowben, "Magnetization at the interface of Cr<sub>2</sub>O<sub>3</sub> and paramagnets with large stoner susceptibility," *J. Phys.: Condens. Matter* **29**, 10LT01 (2017).
- 45. Q. M. Shao, Y. W. Liu, G. Q. Yu, S. K. Kim, X. Y. Che, C. Tang, Q. L. He, Y. Tserkovnyak, J. Shi and K. L. Wang, "Topological Hall effect at above room temperature in heterostructures composed of a magnetic insulator and a heavy metal," *Nat. Electronics* 2, 182 (2019).
- 46. A. S. Ahmed, A. J. Lee, N. Bagués, B. A. McCullian, A. M. A. Thabt, A. Perrine, J. R. Rowland, M. Randeria, P. C. Hammel, D. W. McComb and F. Y. Yang, "Spin-Hall Topological Hall Effect in Highly Tunable Pt/Ferrimagnetic-Insulator Bilayers," *Nano Letters* 19, 5683 (2019).

## **Figure Captions:**

**Figure 1.** (a)  $2\theta/\omega$  XRD scans of a 30 nm Cr<sub>2</sub>O<sub>3</sub> epitaxial film grown on Al<sub>2</sub>O<sub>3</sub>(0001) and Al<sub>2</sub>O<sub>3</sub>(11 $\bar{2}$ 0) substrates. (b) XRD rocking curve of the Cr<sub>2</sub>O<sub>3</sub> (0006) peak for the film on Al<sub>2</sub>O<sub>3</sub>(0001). (c) XRR scan of a 30 nm Cr<sub>2</sub>O<sub>3</sub> film on Al<sub>2</sub>O<sub>3</sub>(0001), where the fitting (black curve) gives a Cr<sub>2</sub>O<sub>3</sub> thickness of 30 nm and a roughness of 0.1 nm. (d) AFM image of a 30 nm Cr<sub>2</sub>O<sub>3</sub> film on Al<sub>2</sub>O<sub>3</sub>(0001) with a surface roughness of 0.1 nm. (d) STEM image of a 30 nm Cr<sub>2</sub>O<sub>3</sub> film on Al<sub>2</sub>O<sub>3</sub>(0001).

**Figure 2**. Topological Hall (TH) measurements of a Pt(2 nm)/Cr<sub>2</sub>O<sub>3</sub>(5 nm) bilayer on Al<sub>2</sub>O<sub>3</sub>(0001). (a) Hall resistivity  $\rho_{xy}$  of Pt(2 nm)/Cr<sub>2</sub>O<sub>3</sub>(5 nm)/Al<sub>2</sub>O<sub>3</sub>(0001) at 345 K, where the black curve is the fitting for  $\rho_{AH}$  with Langevin function and linear background due to  $\rho_{OH}$ . (b) TH resistivity after subtraction of the fitting curve for  $\rho_{AH}$  and  $\rho_{OH}$  in (a). (c)  $\rho_{xy}$  -  $\rho_{OH}$  at various temperatures from 250 to 385 K, where the black curves are the fitting for  $\rho_{AH}$  with Langevin function. (d)  $\rho_{TH}$  after subtraction of the fitting curve for  $\rho_{AH}$  in (c) at each temperature. Inset:  $\rho_{TH}$  as a function of temperature.

**Figure 3**. (a) Hall resistivity  $ρ_{xy}$  -  $ρ_{OH}$  of Pt(2 nm)/Cr<sub>2</sub>O<sub>3</sub>(t) bilayers on Al<sub>2</sub>O<sub>3</sub>(0001) at 345 K with different thickness (t) of Cr<sub>2</sub>O<sub>3</sub>, where the black curves are the fitting for  $ρ_{AH}$  with Langevin function. (b)  $ρ_{TH}$  of the bilayers after subtraction of the fitting curve in (a). (c)  $ρ_{TH}$  as a function of Cr<sub>2</sub>O<sub>3</sub> thickness measured at 345 K. (d) Monte-Carlo simulations of field dependence of topological charges Q at  $T = 1.05T_N$  ( $K = |J_1| = 1$  and  $D = 0.5|J_1| = 0.5$  with out-of-plane easy axis anisotropy). (e) Contour plot of  $ρ_{TH}$  of Pt(2 nm)/Cr<sub>2</sub>O<sub>3</sub>(t) bilayers on Al<sub>2</sub>O<sub>3</sub>(0001) as a function of temperature and Cr<sub>2</sub>O<sub>3</sub> thickness. (f) Contour plot of topological charges Q as a function of temperature  $T/T_N$  and 1/D based on Monte-Carlo simulation. The red circles in (e) and (f) are the data points.

**Figure 4**. (a) Hall resistivity  $\rho_{xy}$  -  $\rho_{OH}$  of a Pt(2 nm)/Cr<sub>2</sub>O<sub>3</sub>(5 nm) bilayer on Al<sub>2</sub>O<sub>3</sub>(11 $\bar{2}$ 0) at various temperatures from 250 to 345 K, where the black curves are the fitting for  $\rho_{AH}$  with Langevin function. (b) TH resistivity  $\rho_{TH}$  after subtraction of the fitting curve for  $\rho_{AH}$  in (a) at each temperature. Inset:  $\rho_{TH}$  as a function of temperature.

Figure 5. (a) Hall resistivity  $ρ_{xy}$  -  $ρ_{OH}$  of Pt(2 nm)/Cr<sub>2</sub>O<sub>3</sub>(t) bilayers on Al<sub>2</sub>O<sub>3</sub>(11 $\bar{2}$ 0) at 345 K with different Cr<sub>2</sub>O<sub>3</sub> thicknesses where the black curves are the fitting for  $ρ_{AH}$  with Langevin function. (b)  $ρ_{TH}$  of the bilayers after subtraction of the fitting curve in (a). (c)  $ρ_{TH}$  as a function of Cr<sub>2</sub>O<sub>3</sub> thickness measured at 345 K. (d) Monte-Carlo simulations of field dependence of topological charges Q at  $T = 1:05T_N$  ( $K = |J_1| = 1$  and D = 0.5  $|J_1| = 0.5$  with easy in-plane anisotropy). (e) Contour plot of  $ρ_{TH}$  of Pt(2 nm)/Cr<sub>2</sub>O<sub>3</sub>(t) bilayers on Al<sub>2</sub>O<sub>3</sub>(11 $\bar{2}$ 0) as a function of temperature and Cr<sub>2</sub>O<sub>3</sub> thickness. (f) Contour plot of topological charges Q as a function of temperature  $T/T_N$  and 1/D based on Monte-Carlo simulation. The red circles in (e) and (f) are the data points.

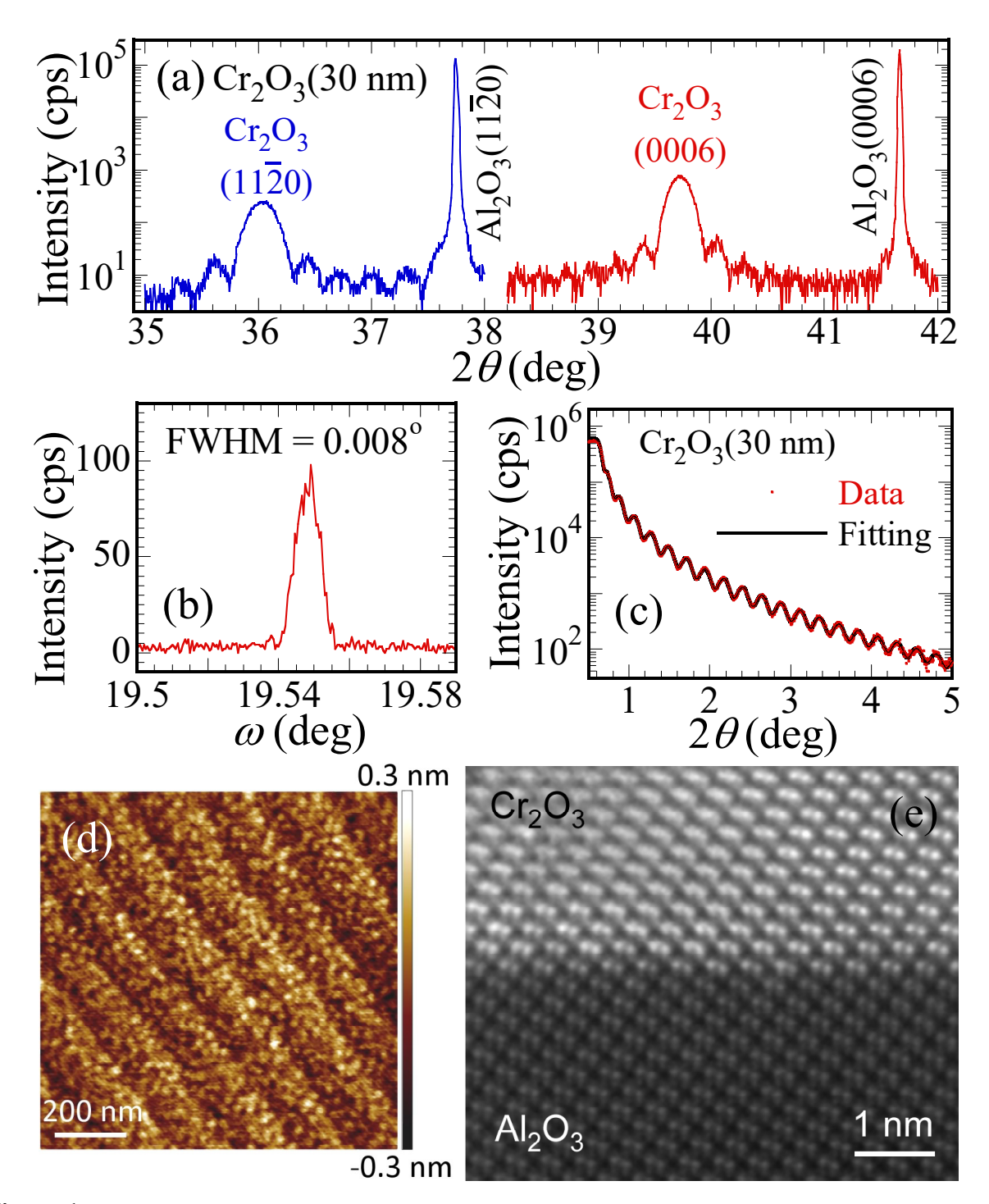


Figure 1.

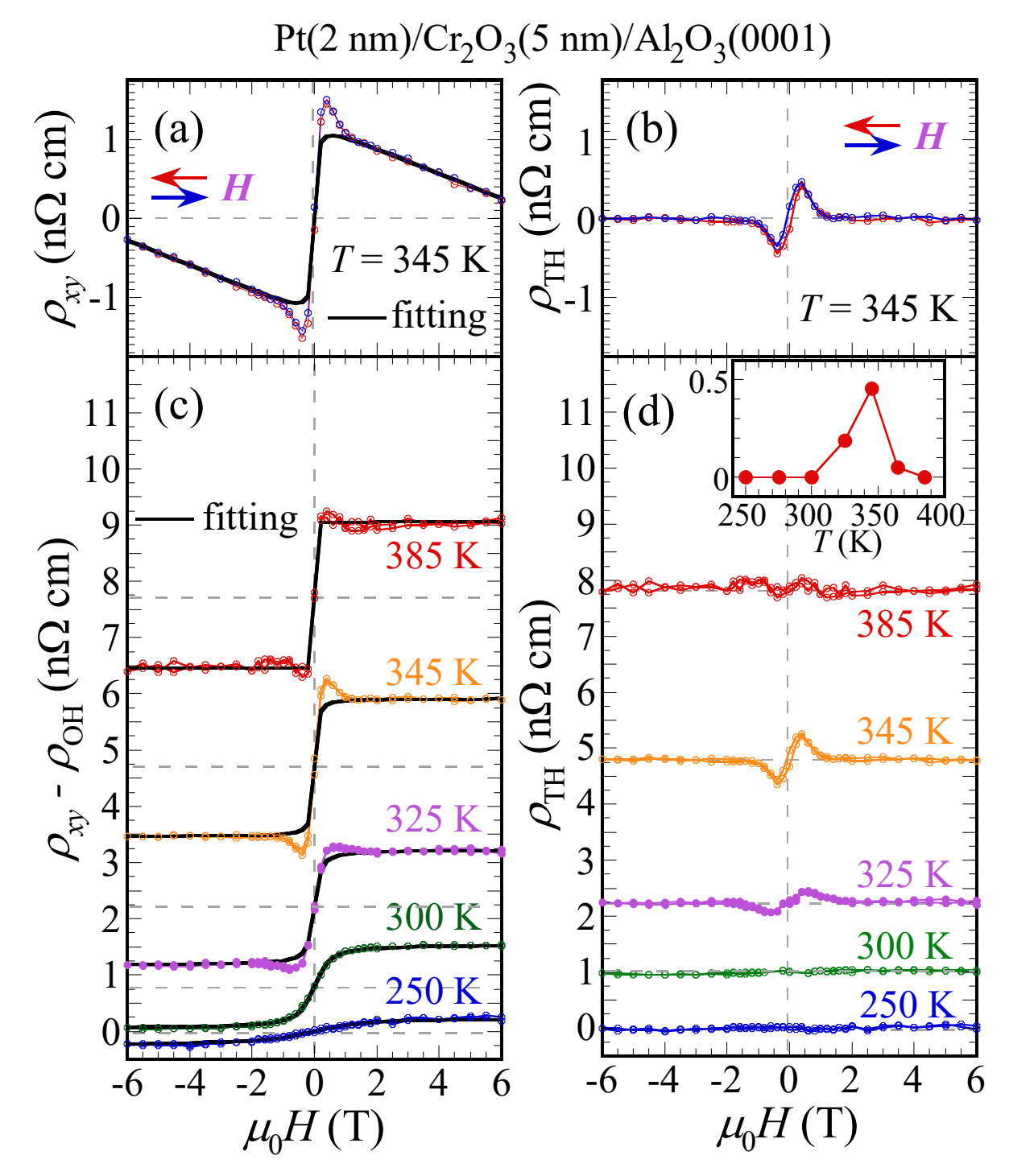


Figure 2.

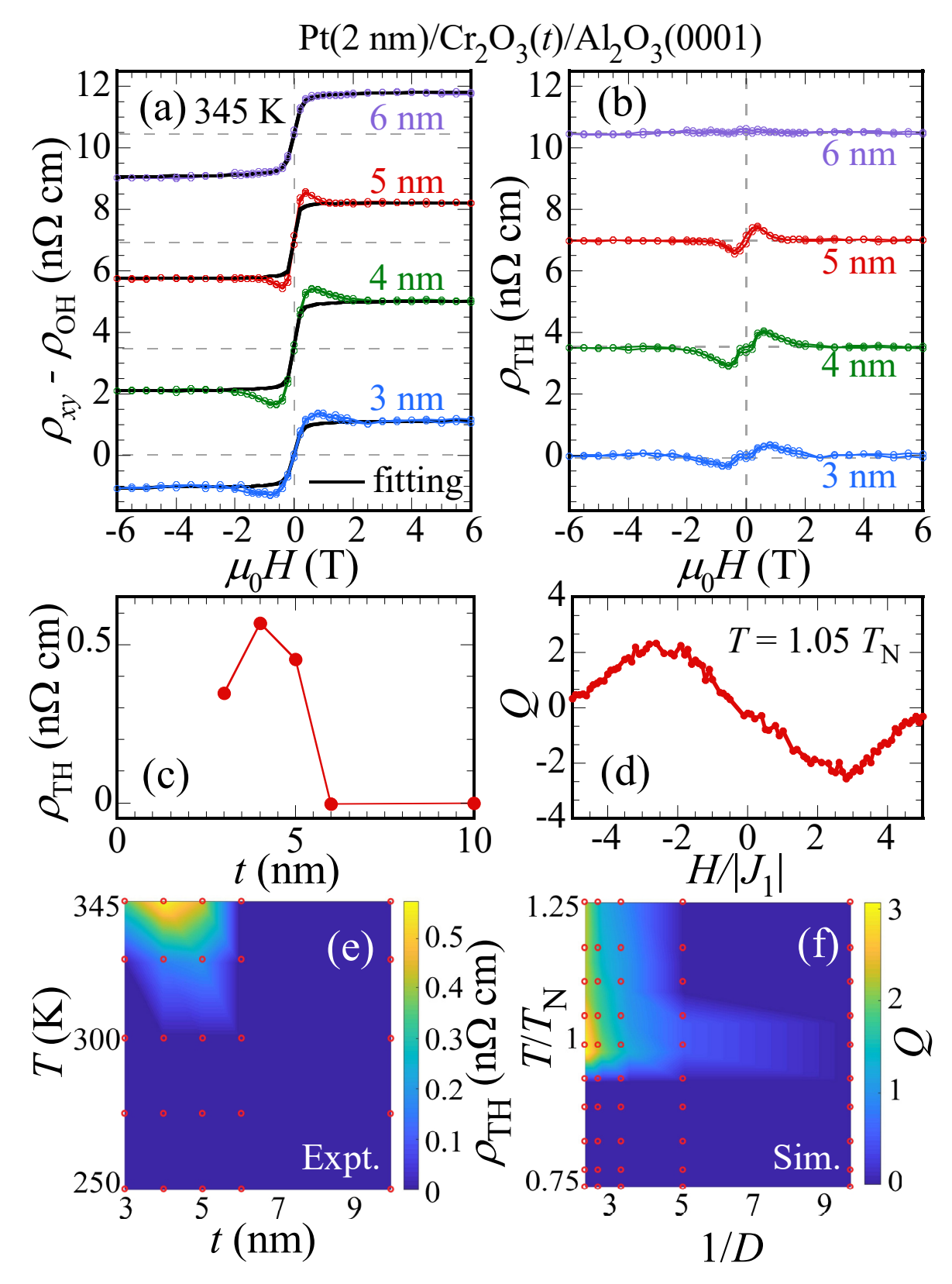


Figure 3.

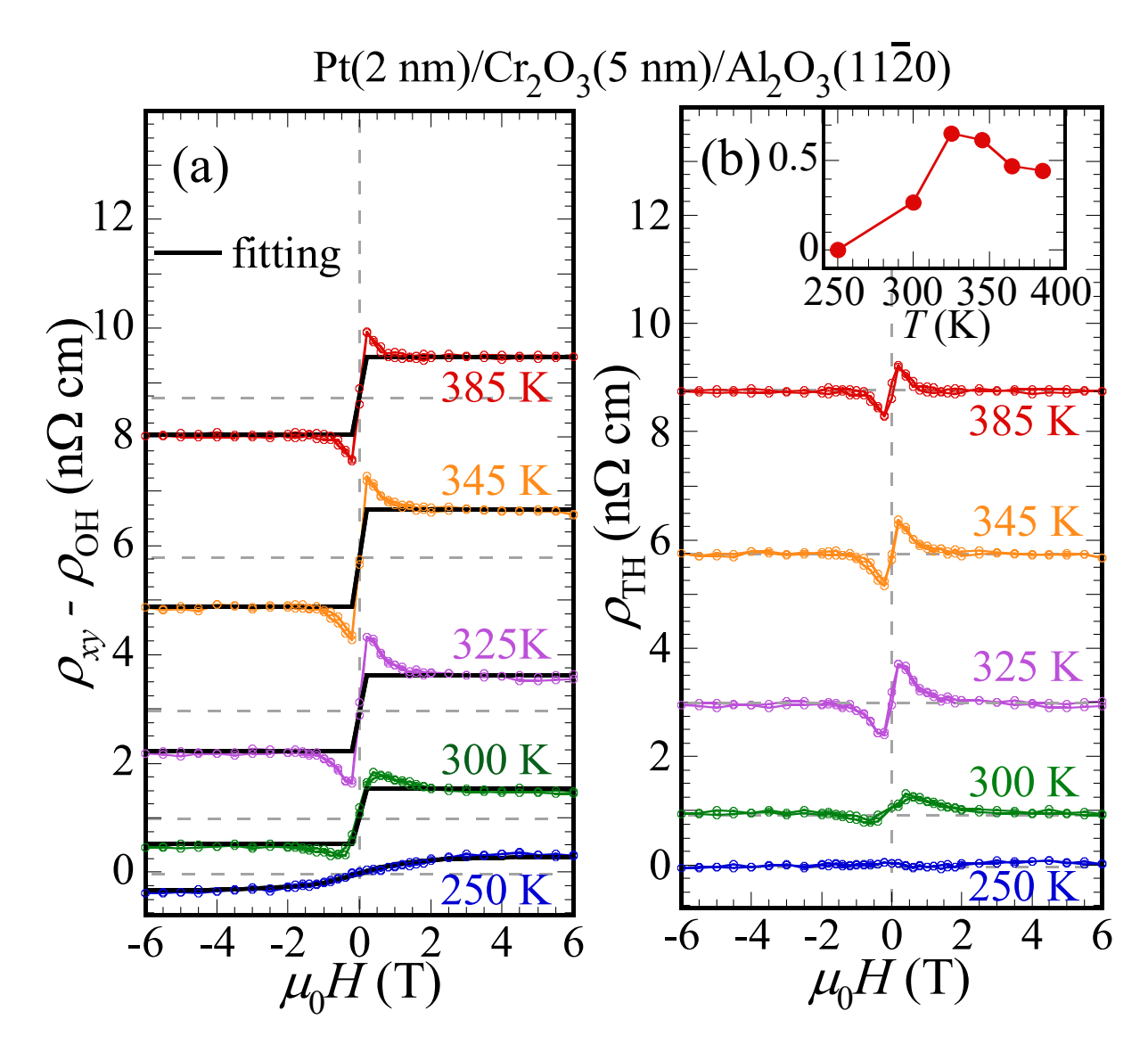


Figure 4.

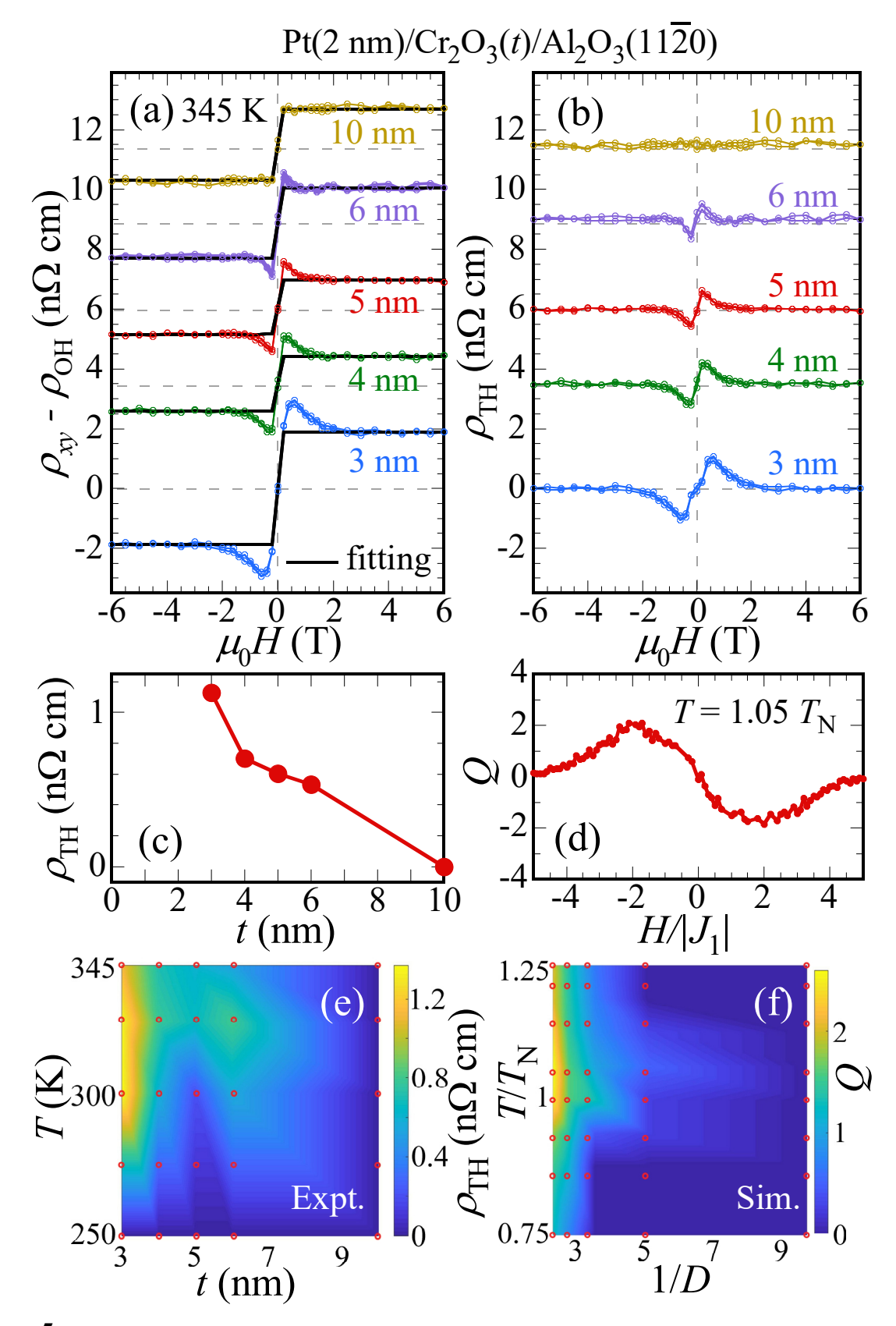


Figure 5.